

JOURNAL OF MECHANICS OF CONTINUA AND MATHEMATICAL SCIENCES www.journalimems.org



ISSN (Online): 2454-7190 Vol.-20, No.-10, September (2025) pp 42-69 ISSN (Print) 0973-8975

PERFORMANCE EVALUATION OF SINGLE-PHASE GRID-TIED SOLAR INVERTER FOR ENHANCED OPERATION CAT MOUSE BASED OPTIMIZATION BASED HYBRID FAST FUZZY-2-DEGREE-OF-FREEDOM FRACTIONAL ORDER TILT INTEGRAL DERIVATIVE REGULATION

Anupama Subhadarsini^{1*}, Babita Panda², Byamakesh Nayak³

^{1,2,3} School of Electrical Engineering, KIIT deemed to be University, Bhubaneswar, India.

Email ID: ¹subhadarshiniannupama@gmail.com, ²babitapfel@kiit.ac.in bnayakfel@kiit.ac.in³

Corresponding Author: Anupama Subhadarsini

https://doi.org/10.26782/jmcms.2025.10.00004

(Received: April 06, 2025; Revised: September 02, 2025; September 20, 2025)

Abstract

This manuscript aims to formulate an innovative approach based on Cat Mouse Based Optimization (CMBO) integrated with a Hybrid Fast Fuzzy-2-Degreeof-Freedom Fractional-Order Tilt Integral Derivative Controller (CMBO-HFF-2DoF-FOTIDC) aimed at enhancing the performance of Grid-Interfaced Solar Inverter Systems (GISIS) while reducing total harmonic distortion. The proposed solar inverter system comprises several elements, including a photovoltaic array, a Relift Luo Converter (RLC), and a 15-Level Switch-Minimized Multilevel Inverter (15L-SMMI), alongside the CMBO-HFF-2DoF-FOTIDC controller. The choice of the RLC over the others from the category stems from its capability to mitigate parasitic capacitance effects, achieve high efficiency, increase power density, reduce ripple voltage magnitude, and lower duty cycle requirements. This control strategy employs a fuzzy-logic-based, optimized 2DoF fractional-order tilt integral derivative controller (2DoF-FOTIDC). The CMBO algorithm optimizes the controller's parameters. Comparative analysis of the CMBO-HFF-2DoF-FOTIDC controller with other state-of-the-art controllers demonstrates its superior performance and effectiveness. Additionally, the manuscript explores the implementation of the Random Pulse Position Pulse Width Modulation (RPPPWM) method alongside the proposed approach. The proposed GISIS aims to address harmonic distortions reduction, alongside improvements in the performance of the solar inverter, robustness, stability, and enhanced capabilities to deal with system uncertainties.

Keywords: CMBO-HFF-2DoF-FOTIDC, CMBO; RLC, robustness; 15L-SMMI, RPPPWM.

I. Introduction

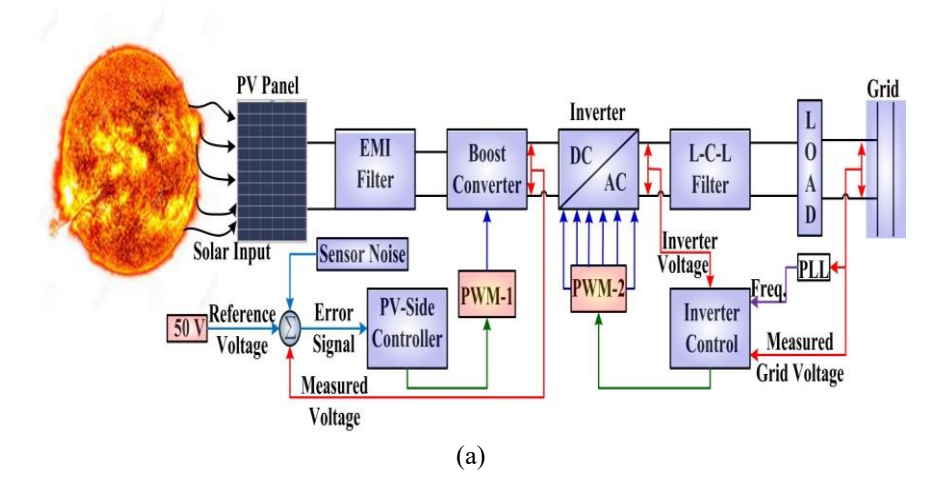
The proposed system incorporates several key components, including the solar photovoltaic array, RLC, 15L-SMMI, and CMBO-HFF-2DoF-FOTIDC controller. The selection of the RLC instead of conventional boost converters is based on its capacity to alleviate the impacts of parasitic capacitance, attain elevated efficacy, enhance power compactness, lessen the magnitude of voltage fluctuations, and demand a reduced duty cycle. In this setup, Insulated-Gate-Bipolar-Transistors (IGBTs) serve as controlled switching devices within the RLC. The CMBO-HFF-2DoF-FOTIDC controller is designed to provide triggering pulses to these IGBTs, facilitating the operation of the RLC. Various techniques for pulse generation have been explored in the literature, including the utilization of Artificial Neural Networks (ANN), Artificial Neuro-Fuzzy Interface Systems (ANFIS), Hysteresis control, and DSP-based controllers, among others [I]. Each of these methods offers unique advantages and trade-offs, contributing to the diverse range of approaches available for pulse generation in solar inverter systems. The selection of the hybrid fuzzy-based fractional order controller stems from its capability to mitigate chaotic behavior in scientific models, enhance system stability, and bolster robustness, thus demonstrating superior dynamic response [II]. Building upon the Tilt-Integral-Derivative (TID) controller, the proposed CMBO-HFF-2DoF-FOTIDC addresses the limitations of TID, namely its slow response to disturbances and lack of robustness [III]. The HFF-2DoF-FOTIDC addresses the limitations of the TID controller. This approach is novel, as there are no documented applications that combine fractionalorder calculus, control theory, and fuzzy control methods in this way. Consequently, a novel control strategy, the CMBO-HFF-2DoF-FOTIDC, is devised for the GISIS. The optimization settings of the CMBO-HFF-2DoF-FOTIDC system are adjusted to achieve the best performance through the CMBO technique [1V], which is modeled after the interaction dynamics observed between felines and rodents in nature. The DC output voltage from the RLC is supplied to the inverter, specifically the 15L-SMMI. The choice of the 15L-SMMI is deliberate, as below 15 levels, harmonic distortions are significant, while beyond 15 levels, switching becomes redundant, limiting the scope for improvement. The adoption of the 15L-SMMI provides benefits like decreased electrical pressure on parts, removal of the necessity for converters, improved electromagnetic coherence, and lowered overall distortion caused by harmonics. The 15L-SMMI system is triggered by the Random Pulse Position Pulse Width Modulation (RPPPWM) technique [V], which controls the pulse width of gating signals for IGBTs in the 15L-SMMI. he examination of stability for the suggested system is performed through analyzing its behavior in terms of frequency using Bode plots, as mentioned in reference [VI]. Additionally, assessments of Total Harmonic Distortion (THD) are carried out in accordance with the criteria specified by IEEE-519 standards, as indicated in reference [VII]. The distinguishing feature of the proposed GISIS resides in its advancement in stability, reinforcement of robustness, elevation in accuracy, superior capability in mitigating harmonics, and increased adeptness in managing uncertainties. The recommended integration of a single-phase solar inverter system with CMBO-HFF-2DoF-FOTIDC contributes significantly to these fundamental aspects, detailed below [VIII].

- A model for GISIS is created using software that simulates conditions to analyse its performance.
- A method for controlling a system, referred to as CMBO-HFF-2DoF-FOTIDC, combined with RPPPWM, is devised for the GISIS to enhance its operation and decrease distortion in signals.
- The effectiveness of the proposed GISIS in reducing signal distortion is supported by evaluating its performance.
- The strength and ability to reduce noise and reinforcement of the robustness of the CMBO-HFF-2DoF-FOTIDC-based GISIS are improved.
- The effectiveness of the CMBO-HFF-2DoF-FOTIDC-based GISIS is confirmed by comparing it with other established methods.

The paper is structured in the following manner. In Section 2, the mathematical representation of all components of GISIS is presented, along with an examination of the proposed GISIS without feedback control. Moving forward, Section 3 elaborates on the mathematical representation of the control method under consideration, referred to as CMBO-HFF-2DoF-FOTIDC. Section 4 delves into the analysis of outcomes and the process of confirming the enhancement in performance and robustness. Lastly, Section 5 provides final remarks on the findings of the paper.

II. Problem Formulations

GISIS encompasses 15L-SMMI, solar cell, RPPPWM-based trigger circuitry, CMBO-HFF-2DoF-FOTIDC, and RLC. Figure 1(a) illustrates the comprehensive GISIS block diagram. The simulation model of the proposed model is presented in Figure 1(b). The GISIS is meticulously modeled in the following subsections [IX].



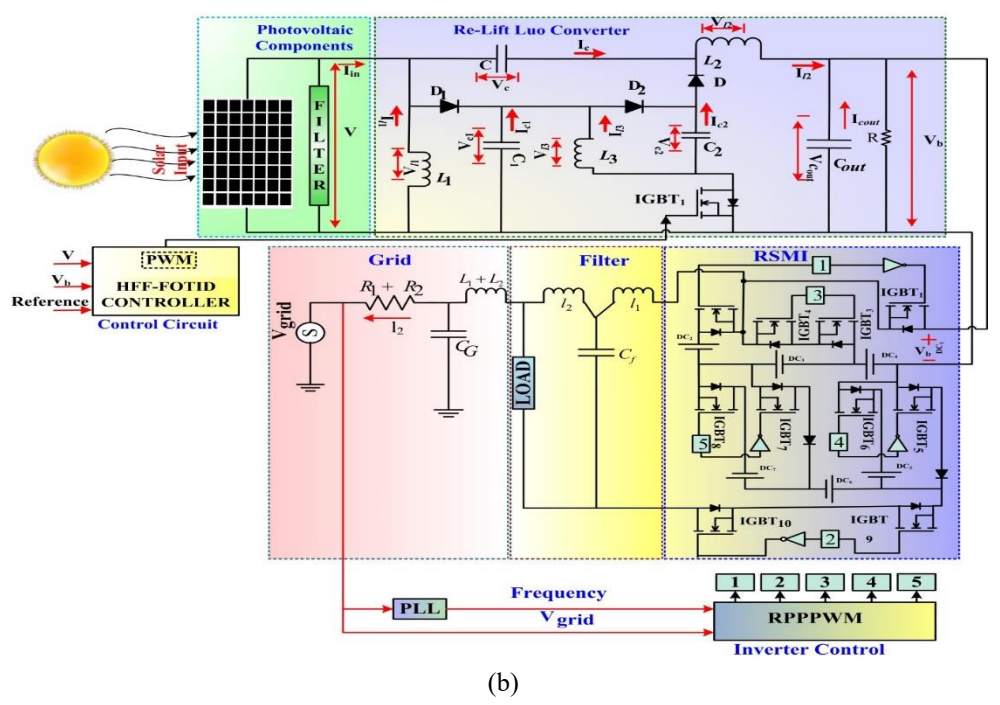


Figure 1 (a) Mathematical prototype of CMBO-HFF-2DoF-FOTIDC tuned GISIS; (b) Schematic illustration of GISIS.

Figure 1(a) presents the mathematical prototype of the Cat Mouse Based Optimization (CMBO)-tuned Hybrid Fractional-Order Fuzzy Two-Degree-of-Freedom Tilted Integral Derivative Controller (HFF-2DoF-FOTIDC) applied to a Grid-Integrated Smart Inverter System (GISIS). The CMBO algorithm optimally adjusts the controller parameters to enhance the system's stability, dynamic performance, and robustness against grid disturbances. The mathematical model outlines the interaction between the CMBO algorithm, fuzzy logic-based hybrid tuning, and fractional-order control elements to achieve superior transient and steady-state responses [X].

Figure 1(b) provides a schematic illustration of the GISIS, detailing its essential components, including the power electronic inverter, control loops, and grid integration framework. This schematic visually represents how the optimized controller enhances the system's ability to regulate voltage, maintain frequency stability, and manage power flow efficiently within the smart grid. By leveraging the CMBO-tuned HFF-2DoF-FOTIDC, GISIS improves dynamic adaptability, reduces voltage fluctuations, and ensures smooth energy exchange between the inverter and the power grid [XI].

II.i. Solar Cell

Solar panels harness energy through a process known as the photovoltaic effect, which relies on factors such as solar irradiance (irr), the short circuit current (I_{Short}), the no load voltage (V_{open}), and the maximum power point. The equivalent setup of a solar panel, which is depicted mathematically, uses Equation (1). The

behavior of a solar panel system comprising multiple or individual units is represented scientifically through Equation (2) [XII].

$$I_{t} = I_{photo} - I_{rs} \left[exp \left(\frac{q_{c} V_{dt}}{akT} \right) \right]$$
 (1)

$$I_{t} = \frac{R_{leakage}}{R_{series} + R_{leakage}} \left[I_{photo} - I_{rs} \left[exp \left(\frac{V_{dt} + R_{series}}{d_{if} V_{ter}} \right) - I \right] - \left(\frac{V_{dt}}{R_{leakage}} \right) \right]$$
(2)

where I_t , I_{photo} , I_{rs} , T, $d_{if} = 1.3$, q_c , R_{Series} , $R_{leakage}$, V_{ter} , k, and V_{dt} denotes the output current, maximum saturation current in reverse mode, temperature in 0 K, diode identity factor, electron's charge, resistance of series arm, resistance of parallel arm, terminal voltage, Boltzmann factor, and diode voltage respectively. Superlatively $I_{Short} >> I_{Photo}$, it is valid as the values of R_{Series} are lower than $R_{leakage}$. Solar irradiance and temperature govern the magnitude of I_{photo} ; it is mathematically expressed in Equation (3), and the I_{rs} is manifested in Equation (4).

$$I_{photo} = \left(\frac{R_{Series} + R_{leakage}}{R_{leakage}} I_{Short} + K_{Sct} T_{c}\right) \frac{irr}{irr_{n}}$$
(3)

$$I_{rs} = \frac{I_{Short} + K_{sct}T_{c}}{exp\left(\frac{V_{open} + K_{vtc}T_{c}}{d_{if}V_{ter}}\right) - 1} \left(\frac{T_{nom}}{T}\right)^{3} exp\left[\frac{q_{c}E_{bg}}{d_{if}k}\left(\frac{1}{T_{nom}} - \frac{1}{T}\right)\right]$$

$$(4)$$

Where the factors of short-circuit temperature, voltage-temperature ratio, temperature variation in Kelvin, solar nominal irradiation in kilowatts per square meter, band gap energy, and nominal temperature are denoted by K_{sct} , K_{vtc} , T_c , irr_n , E_{bg} , and T_{nom} respectively. Upon substituting in Equation (1), the values of I_{photo} and I_{rs} the improved expression for I_t are depicted by Equation (5) [XIII].

$$I_{t} = \frac{R_{leakage}}{R_{Series} + R_{leakage}} \left[I_{photo} - I_{rs} \left[exp \left(\frac{V_{dt} + R_{Series}}{d_{if} V_{ter}} \right) - I \right] - \left(\frac{V_{dt}}{R_{leakage}} \right) \right]$$
 (5)

II.ii. DC-DC Converter

In Figure 1(b), there is a depiction of the model for the RLC. This converter is favored over the same from categories due to the aforementioned capacity towards mitigation of the impact of parasitic capacitance, achieving great efficacy, maintaining great compactness, minimizing ripple voltage level, and operating with reduced operation ratios. Detailed discussion on the RLC is provided in the subsequent subsections [XIV].

II.ii.a. **Design of RLC**

RLC is a category of series RLC, which is developed to overcome the disadvantages of the classical boost converter. Figure 1 (b) contains the model for RLC. An RLC consists of four semiconductor switches (IGBT₁, D, D₁ and D₂), three inductors (L_1, L_2 and L_3), and four capacitors (C_1 , C, C_{out} and C_2). The current from the solar panel is represented by I_{in} . The voltage across the solar panels is V. The current through L_1, L_2 $I_{l_1}, I_{l_2}, I_{l_3}, I_{l_4}, I_{l_5}$ and I_{l_6} respectively. The voltage through L_1, L_2, L_3, C_1, C and C_2 are represented by $V_{l1}, V_{l2}, V_{l3}, V_{c1}, V_{c}$ and V_{c2} respectively. The capacitor C_1 performs the primary task of lifting the capacitor voltage V_{c1} to V volts. When the switch is on, the current from the supply side is given by Equation (6) [XV].

$$I_{in} = I_{l1} + I_{l2} + I_{l3} + I_{C1} + I_{C2} \tag{6}$$

The inductor L_1 , L_3 tends to absorb energy from the solar PV panels. The L_2 engrosses energy as of PV panels and C respectively. When the switches ($IGBT_1$) are off, then $I_{in} = 0$, I_{l1} flows through C_1 and C_3 . Then it flows through the capacitor C_2 and diode D to charge the capacitor C. I_{l2} flows through C_{out} and R, C_1 , L_3 and then through C_2 and D to keep RLC in continuous conduction mode. Presumptuous C_1 as well as C_2 remain adequately outsized besides the voltage across them V_{c1} , and V_{c2} is equal to V in the steady state [XVI].

During switch-ON V_{l3} equals to v, change (peak to peak variation) of I_{l3} is given by Equation (7)

$$\Delta I_{l3} = V \frac{dT}{L_3} \tag{7}$$

At switched—off condition, the reduction in current is expressed by Equation (8).
$$\Delta i_{I3} = \frac{V_{I3}(I-d)T}{I_3}$$
 (8)

The voltage drop across L_3 is given by Equation (9).

$$V_{l3} = \frac{d \times V}{l - d} \tag{9}$$

During switching, the current I_{l1} and I_{l2} are seen to increase during the on-time and decrease during switch-off period, so the voltage applied across the capacitor C can be expressed in terms of the voltage developed across IGBT₁. This relationship is expressed mathematically by Equation (10-11), respectively.

$$V_{IGBT} = \frac{(1-d)(V_c - 2V_{IGBT} - V_{13})}{d}$$
 (10)

$$V_C = \frac{2}{(I-d)} V_{IGBT} \tag{11}$$

The output voltage (V_b) of RLC is given by Equation (12).

$$V_b = \frac{2}{I - k} V_{IGBT} \tag{12}$$

The application of the power balance Equation yields the relationship between the supply current and load current. The mathematical dependency is expressed by Equation (13).

$$P_o = P_{in}$$

$$I_b = \frac{2}{(I-d)} I_s \tag{13}$$

The voltage across C decreases when the switch is closed. The charge across capacitor C increases when the switch is off period. At a charge-balanced condition, the current across all 3 inductors can be expressed with respect to d and I_b . This is expressed mathematically by Equation (14-16).

$$I_{lI} = \frac{d}{I - d} I_{l2} \tag{14}$$

$$I_{lI} = \frac{d}{l_{-d}} I_b = \frac{d}{2} I_{in} \tag{15}$$

$$I_{l3} = I_{l1} + I_{l2} = \frac{1}{1 - d} I_b \tag{16}$$

During the period when the switch is off, the charge across the capacitor C_1 and C_2 decreases, and I_{c1} , I_{c2} is equal to $I_{l1} + I_{l2}$, and is given by Equation (17).

$$I_{c1} = I_{c2} = I_{l1} + I_{l2} = \frac{1}{I - d} I_b \tag{17}$$

During the switch-on period, the average value of currents I_{c1} and I_{c2} are represented in Equation (18)

$$I_{c1} = I_{c2} = \frac{I - d}{d} I_{II} + I_{I2} = \frac{I_b}{d}$$
 (18)

The average value of current from the PV array during the switch-on period is given by Equation (19).

$$I_{in} = I_{l1} + I_{l2} + I_{l3} + I_{c1} + I_{c2}; \quad I_{in} = 2d\left(I_{l1} + I_{l2}\right)\left(I + \frac{I - d}{d}\right); \quad I_{in} = \frac{2}{I - d}I_b; \tag{19}$$

The peak-to-peak variations of I_{l1} and I_{l2} are given by Equation (20), respectively.

$$\Delta i_{l1} = \frac{dTV_s}{L_1}; \quad \Delta i_{l2} = \frac{dTV_s}{L_2}; \quad \Delta i_{l3} = \frac{dTV_s}{L_3};$$
(20)

Similarly, the peak-to-peak variation across output voltage and across the capacitors (C_1 , C_2 and C) is represented mathematically by Equation (21).

$$\Delta V_C = \frac{(1-d)dTI_S}{2C}; \quad \Delta V_b = \frac{dT^2V_S}{8C_{out}L_2}; \quad \Delta V_{CI} = \frac{(1-d)I_S}{2C_If}; \quad \Delta V_{C2} = \frac{(1-d)I_S}{2C_2f};$$
 (21)

Ripple is defined as the residual periodic variation of the DC voltage V_b . The ripple formation is attributed to I_{l1} , I_{l2} , I_{l3} , V_{c1} , V_c , V_{c2} and V_b respectively. Therefore, it is desirable to study the effects of ripple. The value of the supplied voltage from solar panels is 22 volts, and the required output voltage is 50 volts. The value of the duty cycle d is 0.5669. As the variations in the ripple values of I_{l1} and I_{l2} are small so the variations of V_c are even smaller, and the output voltage V_b ripple variations are the smallest. The circuit delivers a clean DC output voltage V_b with minimal ripple due to the resistive load. Component details for this low-ripple solution are provided in Table 1.

Table 1: Parameters of RLC

f	100KHz	C_2	400 μ F
l_1	0.0931mH	C_{out}	400 μ F
l_2	0.0931mH	С	10 μ F
l_3	0.0931mH	C_1	400 μ F
R	50 Ω		

Table 1 illustrates the key parameters of an RLC circuit designed for a low-ripple solution in a Grid-Integrated Smart Inverter System (GISIS). It highlights the circuit's operating frequency (100 kHz), inductors (0.0931 mH) for current ripple reduction, capacitors (400 F, 10 F) for voltage stabilization, and a 50 Ω resistor for damping oscillations. This optimized component selection ensures improved power quality, reduced voltage fluctuations, and enhanced overall system efficiency.

II.iii. 15L-SMMI

This manuscript uses a symmetrical 15-Level Switch-Minimized Multilevel Inverter (15L-SMMI). This configuration is illustrated in Figure 1(b). Unlike the cascaded H-bridge design, there is a significant benefit in its ability to decrease the number of controlled switches while maintaining a constant source requirement, thereby enhancing system performance. Opting for a 15L-SMMI offers several advantages: it lowers components' voltage stress, transformerless circuitry, increases electromagnetic compatibility, and moderates Total Harmonic Distortion (THD) [XVII].

Total switch count =
$$\frac{Level + 5}{2}$$
 (22)

Total source count =
$$\frac{Level-1}{2}$$
 (23)

Where *Level* is the level of the inverter. The equations (22 and 23) establish the criteria for the quantity of switches and sources necessary for a multilevel inverter with reduced switch count. It is apparent from these equations that for a 15L-SMMI, the required number of switches and sources is 10 and 7, respectively. The selection of the proposed inverter technique is motivated by the presence of significant harmonic distortions below this level, while above this level, the switching method encounters challenges with diminished or only marginally enhanced performance.

The IGBTs are labeled sequentially $IGBT_I$ to $IGBT_{I0}$ correspond. Similarly, the sources are designated as DC_1 to DC_7 , respectively. In the proposed method, each of the sources within the reduced switch count multilevel inverter is linked to the RLC.

II.iii.a. Harmonic

The comprehensive assessment of harmonic components inside the current waveform is referred to as total harmonic distortion. Electrodynamic contacts are increasingly used, leading to the generation of harmonics, commonly represented by THD_i . There are various pathways through which harmonics can affect electricity systems. These effects include, but are not limited to, inadvertent triggering of Interrupters, reduced power factors, elevated thermal output, decreased efficiency, and elevated electromagnetic emissions. Maintaining a low value of THD_i is preferable as it diminishes maximum current, enhances power factor, and progresses inclusive efficacy. The IEEE-519 standard offers guidelines for measuring THD_i [XVIII].

II.iv. Random Pulse Position Pulse Width Modulation (RPPPWM)

RPPPWM uses a direct quadrature analysis method to generate the sinusoidal reference signal. The carrier wave is generated by using the Random Pulse Position Pulse Width Modulation (RPPPWM) technique [XVII, XVIII]. In DQC-RPPPWM, the randomized carrier wave, which is a randomized square signal, is compared with a sinusoidal reference generated by the direct quadrature analysis method. In the RPPPWM technique, the carrier wave is switched at 8,500 Hz. However, the position of the gate pulse is randomized within each switching period instead of commencing from the beginning of the cycle. In RPPPWM, the pulses of the carrier signal are randomly positioned in the individual switching period. The randomized frequency is achieved by varying the switching interval of the square wave carrier signal. This is further achieved by varying the width of each signal still keeping the pulse centrally aligned. The formulation of a triggering strategy based on the mathematical network of the CMBO-HFF-2DoF-FOTIDC based GISIS is utilized [XVIII]. $V_{grid} \& V_{inv}$ represents the voltage from the grid and 15L-SMMI. While $i_2 \& i_1$ represents the current from the grid and 15L-SMMI. The 15L-SMMI and the grid are coupled through a conditioning element known as a filter. The resistive element of the filter placed on either interface is represented by R_2 and R_1 respectively. The inductive element of the filter placed on either interface is represented by l_1 and l_2 respectively.

The system incorporates a capacitance element denoted as C_f . A unified mathematical representation of the grid and inverter's interactive behavior is captured in Equations (24-26).

$$V_{inv} = R_1 i_1 + s L_1 i_1 + V_{cf}$$
 (24)

$$V_{cf} = R_2 i_2 + s L_2 i_2 + V_{grid} (25)$$

$$i_1 = i_2 + \frac{V_{cf}}{S} \tag{26}$$

The α and β component of V_{inv} is represented by V_{inv}_{α} as well as V_{inv}_{β} individually. The design of the current controller disregards the influence of C_f . Transitioning to the $\alpha\beta$ frame (Equations 27-28) provides a revised representation of

$$V_{inv} = (R_1 + R_2)i_{\alpha} + s(L_1 + L_2)i_{\alpha} + V_{orid}$$
(27)

$$V_{inv \beta} = (R_1 + R_2)i_{\beta} + s(L_1 + L_2)i_{\beta} + V_{grid \beta}$$
(28)

Equation (29) specifies the values for i_{α} and i_{β} .

Equation (24), offering deeper insights.

$$i_{\alpha} = I_{m} \cos \theta$$

$$i_{\beta} = I_{m} \sin \theta$$
(29)

For computational efficiency, Equation (27-28) undergoes a stationary-to-rotating reference frame transformation, leading to Equation (30).

$$V_{inv_d} = R_1 \times i_d + R_2 \times i_d + s \times L_1 \times i_d + s \times L_2 \times i_d - \omega_{ff} \times L_1 \times i_q - \omega_{ff} \times L_2 \times i_q + V_{grid_d}$$

$$V_{inv_q} = R_1 \times i_q + R_2 \times i_q + s \times L_1 \times i_q + s \times L_2 \times i_q - \omega_{ff} \times L_1 \times i_d - \omega_{ff} \times L_2 \times i_d + V_{grid_q}$$

$$(30)$$

Equation (31) plays a crucial role in understanding the relationship between the grid, inverter, and control signals for voltage $(V_{c_{_}d} \text{ and } V_{c_{_}q})$ in the dq axis. This relationship is governed by the nominal angular frequency (ω_{ff}).

$$V_{inv_{d}} = V_{c_{d}} - \omega_{ff}(L_{1} + L_{2})i_{q} + V_{grid_{d}}$$

$$V_{inv_{q}} = V_{c_{q}} - \omega_{ff}(L_{1} + L_{2})i_{d} + V_{grid_{q}}$$
(31)

 V_{c_d} and V_{c_q} are used to calculate i_d and i_q . They are scientifically stated by way of Equation (32).

$$V_{c_{-}d} = R_1 \times i_d + R_2 \times i_d + s \times L_1 \times i_d + s \times L_2 \times i_d$$

$$V_{c_{-}q} = R_1 \times i_q + R_2 \times i_q + s \times L_1 \times i_q + s \times L_2 \times i_q$$
Equation (33) establishes the mathematical equivalence between fictitious currents

Equation (33) establishes the mathematical equivalence between fictitious currents $(i_{\alpha}^* \text{ and } i_{\beta}^*)$ introduced to aid in the $\alpha\beta - dq$ transformation of single-phase systems.

$$i_{\alpha}^{*} = I^{*} = I_{m}^{*} \cos(\theta_{PLL})$$

$$i_{\beta}^{*} = I_{m}^{*} \sin(\theta_{PLL})$$
(33)

While Equations (34) and (35) both represent transformations between reference frames, Equation (34) specifically handles the conversion from $\alpha\beta - dq$, while Equation (35) performs the reverse operation. Interference distorts the original signal with a phase shift version.

$$\begin{vmatrix} \alpha \\ \beta \end{vmatrix} = \begin{vmatrix} \cos(\theta) & -\sin(\theta) \\ \sin(\theta) & \cos(\theta) \end{vmatrix} \begin{vmatrix} d \\ q \end{vmatrix}$$
 (34)

$$\begin{vmatrix} d \\ q \end{vmatrix} = \begin{vmatrix} \cos(\theta) & \sin(\theta) \\ -\sin(\theta) & \cos(\theta) \end{vmatrix} \begin{vmatrix} \alpha \\ \beta \end{vmatrix}$$
 (35)

Equation (36) leverages the dq transformation with a parameter $\theta = \theta_{PLL}$ to formulate the two reference currents $(i_{\alpha}^* \text{ and } i_{\beta}^*)$ for further analysis or control.

$$i_d^* = I_m^*(\cos^2(\theta_{PLL}) + \sin^2(\theta_{PLL})) = I_m^*$$

$$i_q^* = 0.5 \times I_m^*(-\sin(2 \times \theta_{PLL}) + \sin(2 \times \theta_{PLL})) = 0$$
Adding delays can slow down a system's response. This issue is resolved by the use

Adding delays can slow down a system's response. This issue is resolved by the use of an error signal $(i_{\alpha}^* - i_{\alpha})$ to create a steady-state error in the frame. We represent errors for the direct and quadrature axes as $\mathcal{E}d$ and $\mathcal{E}q$, respectively. Assuming steady-state conditions $(i_{\beta} = i_{\beta}^*)$ exist, Equation (37-38) expresses $\mathcal{E}d$ and $\mathcal{E}q$.

$$\varepsilon d = i_d^* - i_d = [(i_\alpha^* - i_\alpha)\cos(\theta_{PLL})] \tag{37}$$

$$\varepsilon q = i_q^* - i_q = [-(i_\alpha^* - i_\alpha)\sin(\theta_{PLL})] \tag{38}$$

Equations 24-38 define the sinusoidal reference for a modulated pulse signal. This reference, compared with a carrier wave, regulates the triggering states of the RPPWM-based 15L-SMMI. The moment the reference amplitude (V_q) surpasses the carrier amplitude (V_{car}), a positive pulse is generated. Conversely, a negative pulse occurs when V_q falls below V_{car} . Equations (39) and (40) define the 15L-SMMI's modulation index and output voltage (V_{inv}).

$$m_a = \frac{V_q}{V_{car}} \tag{39}$$

$$V_{inv} = V_s \sqrt{\left(\sum_{b=1}^{2n} \frac{2T_{on}}{T \times \pi}\right)} \tag{40}$$

15L-SMMI inverter sets the individual pulse width (T_{on}) based on its switching period. This pattern, depicted in Figure (1), is achieved through the modulation strategy outlined in Equations 24-40.

II.v. Filter

Crucial design parameters for the LCL filter, employed to clean the 15L-SMMI output, are defined in Equations (41-43). These parameters include base values of impedance (Z_b), capacitance (Z_b), and maximum load current (Z_b).

$$z_b = V_{bn}^2 p_l^{-1} (41)$$

$$C_b = \left(\omega_g z_b\right)^{-1} \tag{42}$$

$$I_{max} = 0.333 * P\sqrt{2} * (V_f)^{-1}$$
(43)

Equations (44-45) capture the combined effects of a 10% filter component tolerance and a 10% change in inverter inductance (L_I) on filter voltage (V_f) and active power (P_I) , crucial for robust filter design.

$$L_{I} = \frac{V_{b}}{0.6 \times f_{SW} \times I_{max}} \tag{44}$$

$$\Delta I_{max} = 0.10 \times I_{max} \tag{45}$$

The mathematical relationships governing the inductor (L_2) placed interfacing the grid and shunt arm capacitor (C_f) are captured in Equations (46) and (47), which incorporate the parameters of switching frequency (f_{sw}) and DC link voltage (V_b) .

$$L_{2} = \frac{\sqrt{\left(k_{a}^{-2} + I\right)}}{C_{f} \times \left(f_{sw}\right)^{2}} \tag{46}$$

$$C_f = 0.1 \times C_b \tag{47}$$

where k_a represents the attenuation factor. The use of resistance (R_f) alongside C_f compensates for the ripple effects, electromagnetic interference, and resonance. Equation (48) articulates the scientific similarity for R_f .

$$R_f = \left(\omega_{res} \times 3C_f\right)^{-1} \tag{48}$$

This set of equations (41-48) defines the filtering approach for the GISIS, relying on the resonant frequency (ω_{res}) and visualized in Figure 1(a).

II.vi. Open Loop Response

The forthcoming subsections meticulously examine the solar inverter system's features under a range of operational configurations.

II.vi.a. Open Loop RLC

This work utilizes an IGBT-based converter operating at 30kHz, controlled by a simple pulse generator. The converter elevates the voltage of the solar subsystem from 24V to 44.48V, displaying a fluctuation ranging from $\pm 2.29\%$ (1.01986) Volts. Figure 2(a) illustrates the open-loop output voltage, depicting fluctuations ranging from 43.97V to 45V. These variations predominantly arise due to inherent nonlinearities present in the system.

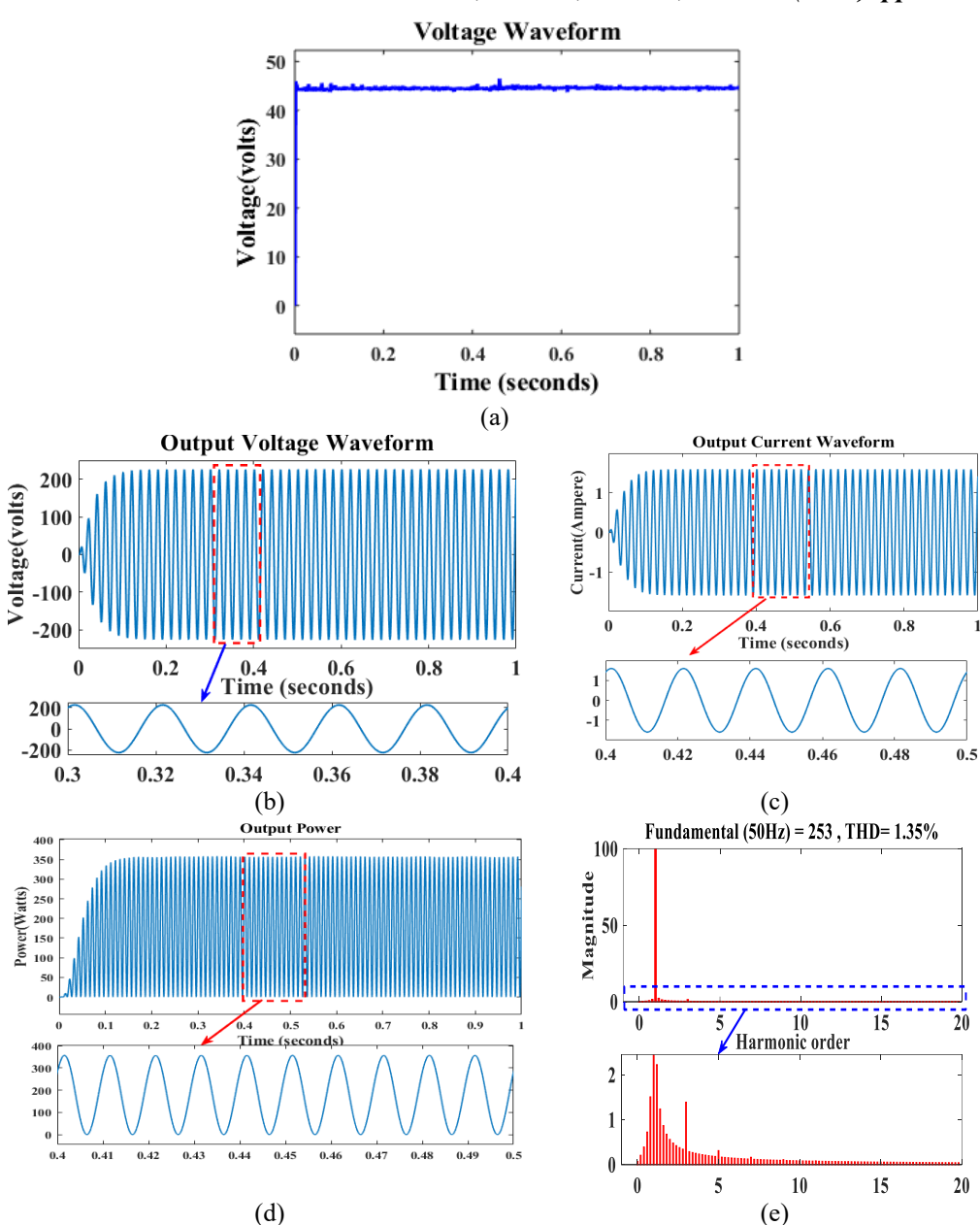


Fig. 2. Open loop parameters of GISIS (a) V_b plot for RLC; (b) V_{inv} plot for 15L-SMMI; (c) I_{inv} plot for 15L-SMMI; (d) P_{inv} plot for 15L-SMMI; (e) thd_i graph

Figure 2(a) presents the open-loop response of the RLC circuit, demonstrating how the system behaves under uncontrolled conditions. This plot highlights the impact of passive components on voltage and current waveforms, emphasizing their role in reducing ripple and stabilizing power flow. The behavior of inductors, capacitors, and resistors in filtering out high-frequency oscillations and ensuring steady-state performance is visually analyzed.

Figure 2(b) illustrates the output characteristics of the 15-Level Symmetric Multilevel Inverter (15L-SMMI) in an open-loop configuration. It depicts how the inverter generates stepped voltage waveforms, which help in reducing harmonic distortion. The plot also provides insights into the voltage levels and their transitions, showing how multilevel inverters improve the quality of power delivered to the grid.

Figure 2(c) continues the analysis of 15L-SMMI, focusing on the harmonic content and distortion levels present in the output waveform. By examining the frequency spectrum, this plot helps evaluate how effectively the inverter minimizes unwanted harmonics, ensuring compliance with power quality standards. Lower total harmonic distortion (THD) values indicate an efficient design suitable for grid integration.

Figure 2(d) further explores the dynamic response of the 15L-SMMI, showcasing transient characteristics such as overshoot, settling time, and response to input variations. The inverter's ability to maintain stable operation during load changes and disturbances is examined, validating its reliability for practical applications in smart grids and renewable energy systems.

Figure 2(e) presents a comparative graph summarizing the performance of different configurations, including the RLC-based circuit and the 15L-SMMI. This visualization highlights improvements in power quality, voltage regulation, and efficiency, offering a comprehensive assessment of the system's overall effectiveness in managing energy flow within the Grid-Integrated Smart Inverter System (GISIS).

II.vi.b. Open Loop 15L-SMMI

The multilevel inverter, with reduced switch count, operates at a switching frequency of 30 kHz generated by the pulse source. Figure 2(b-d) displays the 15L-SMMI's V_{inv} at 226 volts, I_{inv} at 1.5 amperes, and apparent power (P_{inv}) at 340 watts. Figure 2(e) reveals a harmonic distortion (THD_i) of 1.63%. This open-loop analysis demonstrates the need for a control strategy.

III. Control Approach

The subsequent antecedent sections validate the suggested control method (CMAES-CMBO-HFF-2DoF-FOTIDC). This approach combines a fast fuzzy system with a Tilt Integral Derivative Controller (TIDC). The evaluation comprehensively analyzes the effectiveness, precision, and resilience of CMAES-CMBO-HFF-2DoF-FOTIDC. The effectiveness of this hybrid control technique is confirmed by analyzing control performance indices and assessing the harmonic distortion thd_i , V_b , V_{inv} , I_{inv} and P_{inv} [9-13]. The integration of Fast Fuzzy (FF) with the 2DoF-FOTIDC aims to enhance the controller's response, improve the efficiency of fuzzy systems, and reduce data acquisition errors. This fusion results in a robust control method that offers superior performance for non-linear systems. Detailed explanations of the HFF-2DoF-FOTIDC are provided in the appended sub-sections.

III.i. Fast Fuzzy Controller

The controller must address a substantial initial discrepancy, necessitating a swift reaction to mitigate it. This rapid adjustment is achieved by aligning the actuator with

the control signal. This concept is integrated into the Fast Fuzzy Controller (FFC), which is designed with a logical judgment module coupled with a fuzzy controller module. The functioning equation for comparing position error (Err) with the error threshold (th) for the FFC is presented in Equation (49).

$$u_k = \begin{cases} 1 & Err > th \\ 0 & Err \le th \end{cases} \tag{49}$$

Initially, the positional deviation exceeds the error limit. The logical assessment module detects this, outputs a value of 1, and triggers the actuator to increase speed. Conversely, when the output is 0, the FF-TID controller dynamically adjusts the control parameters, enhancing accuracy. FF systems involve converting inputs into fuzzy values, creating the rule base, applying fuzzy logic, and converting fuzzy values back into precise outputs. Inputs and outputs are represented by seven membership functions: NB, NM, NS, ZE, PS, PM, and PB, which represent Negative Big, Negative Medium, Negative Small, Zero, Positive Small, Positive Medium, and Positive Big. These functions form the rule base for the FF system. Figure 3(b) illustrates the error input's membership degree, and Figure 3(c) shows the change in error input's membership degree. Figure 3(d) represents the outputs $(\Delta K_t, \Delta K_i \text{ and } \Delta K_d)$ of the FF system. Figure 3(e) represents the surface plots for the outputs $(\Delta K_t, \Delta K_i \text{ and } \Delta K_d)$ with respect to error and change in error of the FF system. The rule base, detailed in Table 2, links input and output membership functions during fuzzy inference. In the defuzzification phase, outputs are translated into precise values using the mean of maxima technique.

Table 2: Fuzzy Logic Rule Table

	Error (E)								Error (E)						Error (E)								
	ΔK_t	NB	NM	NS	ZE	PS	PM PB]	ΔK_i	NB	NM	NS	ZΕ	PS	PM PB	ΔK_d	NB	NM	NS	ZE I	PS P	M	PB
	NB		B	Pl	M	PS	ZE		NB	N	ΙB	N1	M	NS	ZE	NB	PS	NS		NB	N	ΙM	PS
	NM	1	D	PM	DC	PS	ZE NS		NM			NM	NS			NM			NB	NN	I N	IS	ZE
Rate of	NS	D.	NΓ	PIVI	Po	ZE	NS		NS	NB	NM	NS		ZΕ	PS	NS	ZE	NS	NN	Λ	NS	5	
change of	ZE	PM		PS	ZE	NS	NM		ZE	NM			ZΈ	PS	PM	ZE				NS			
error	PS	PS PS		ZE	N	IS	INIVI		PS		NS	ZE	PS	S		PS	ZE						
	PM	PS ZE		NS		NM	NB		PM ZE		PS :		PM	PB	PM	PB NS PS			PB				
	PB	B ZE NM			NB NB		PB		PS	P	M		PB		NM	PΝ	Л	PS	5				

Table 2 illustrates the Fuzzy Logic Rule Table, which defines the control strategy for the Grid-Integrated Smart Inverter System (GISIS) by mapping input variables to appropriate output responses. The table consists of fuzzy linguistic terms such as Negative Large (NL), Negative Medium (NM), Negative Small (NS), Zero (Z), Positive Small (PS), Positive Medium (PM), and Positive Large (PL) to represent variations in system parameters. The fuzzy rules are formulated based on expert knowledge, ensuring optimal decision-making for voltage regulation, stability enhancement, and ripple minimization. By applying these rules, the fuzzy logic controller dynamically adjusts system behavior, improving the efficiency and robustness of GISIS under varying operating conditions.

III.ii. 2-Degree-of-Freedom Fractional Order Tilt Integral Derivative Controller (2DoF-FOTIDC)

The 2-Degree-of-Freedom Fractional Order Tilt Integral Derivative Controller (2DoF-FOTIDC) is a sophisticated control system designed to optimize performance by integrating two distinct degrees of freedom. This controller regulates and stabilizes systems through effective management of the integral and derivative components associated with tilt or angular position. Unlike conventional controllers, the 2DoF-FOTIDC employs fractional-order dynamics, enabling a more refined and adaptable response to system behavior.

The integral component addresses long-term discrepancies, ensuring steady-state precision, while the derivative component responds to the rate of change in the system, aiding in damping oscillations and enhancing stability. The fractional-order feature introduces a fractional exponent into the mathematical model, allowing for tailored tuning of the controller's response to meet the specific needs of the system. In the suggested control method, the system takes the deviation (E) and the rate of deviation change (ΔE) as inputs to the fractional-order model. The 2DoF-FOTIDC has two inputs and one output (Controller(s)). One input comes from the fractional-order system's result, and the other uses a reference value. The system's output is fed into the 2DoF-FOTIDC controller, designed similarly to a PID controller. The tilt gain, acting as the proportional component, is applied via a tilt function aimed at enhancing system stability. The transfer functions of the 2DoF-FOTIDC controller are given in Equation (50).

$$\frac{Error(s)}{Controller(s)} = TW \times \frac{K_t}{s^{(-n)}} + \frac{K_i}{s^{\alpha}} + DW \times K_d \frac{s^{\beta} \times N}{s^{\beta} + N}$$

$$\frac{Y(s)}{Controller(s)} = \frac{K_t}{s^{(-n)}} + \frac{K_i}{s^{\alpha}} + K_d \frac{s^{\beta} \times N}{s^{\beta} + N}$$
(50)

Where TW, DW, K_t , K_i , K_d , n, α and β represent tilt gain compensation, derivative gain compensation, gain of tilt function, gain of integral function, gain of derivative function, tilt coefficient, integral coefficient as well and derivative coefficient. The control parameters are optimized using a fitness function, specifically ITAE, to reduce system error, as depicted in Equation (51).

$$ITAE = \int_0^\infty t \times |e_{rr}(t)| dt \tag{51}$$

where $|e_{rr}(t)|$ denotes the magnitude of the error signal.

III.iii. Fast Fuzzy – Fractional Order Tilt Integral Derivative Controller (HFF-FOTID)

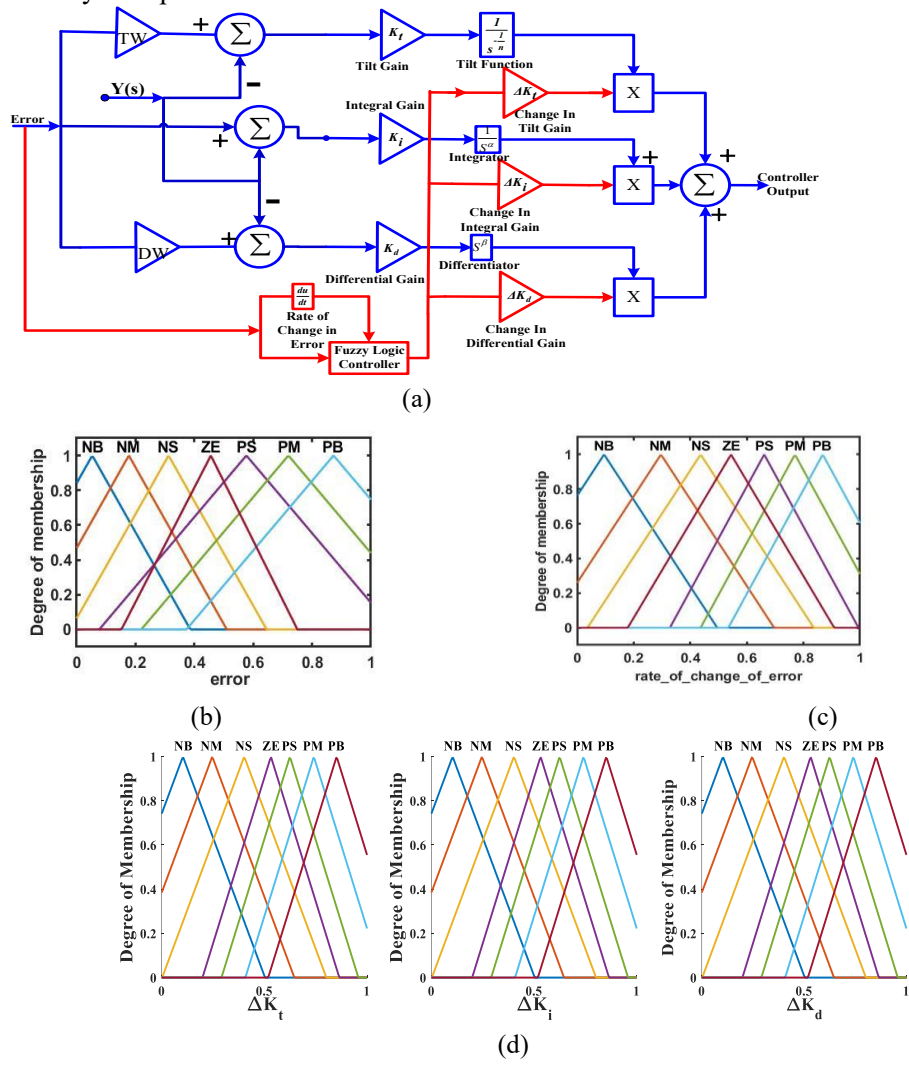
Given the superior performance of both FF and TIDC equated with other control approaches, their amalgamation is predictable to deliver superior performance. This expectation is confirmed in the results and discussion section (Section 4) of the manuscript. Figure 3(a) presents the transfer function model of the HFF-2DoF-FOTIDC. The inputs to the HFF-2DoF-FOTIDC are the outputs from FF, denoted as ΔK_t , ΔK_i and ΔK_d . These inputs are multiplied by the corresponding constraints of FOTIDC. The control signal output from the HFF-FOTIDC is referred to as

 $U_{Controller}(s)$. Equation (52) represents the overall transfer function (T(s)) for the HFF-2DoF-FOTIDC.

$$T(s) = \begin{cases} \frac{Error(s)}{U_{Controller}(s)} = TW \times \frac{\Delta K_t \times K_t}{s^{(-n)}} + \frac{\Delta K_i \times K_i}{s^{\alpha}} + DW \times \Delta K_d \times K_d \frac{s^{\beta} \times N}{s^{\beta} + N} \\ \frac{Y(s)}{U_{Controller}(s)} = \frac{\Delta K_t \times K_t}{s^{(-n)}} + \frac{\Delta K_i \times K_i}{s^{\alpha}} + \Delta K_d \times K_d \frac{s^{\beta} \times N}{s^{\beta} + N} \end{cases}$$

$$(52)$$

The control parameters of HFF-2DoF-FOTIDC are optimized using CMAES-CMBO to minimize error. This technique is also used to estimate GISIS control parameters for enhanced system performance.



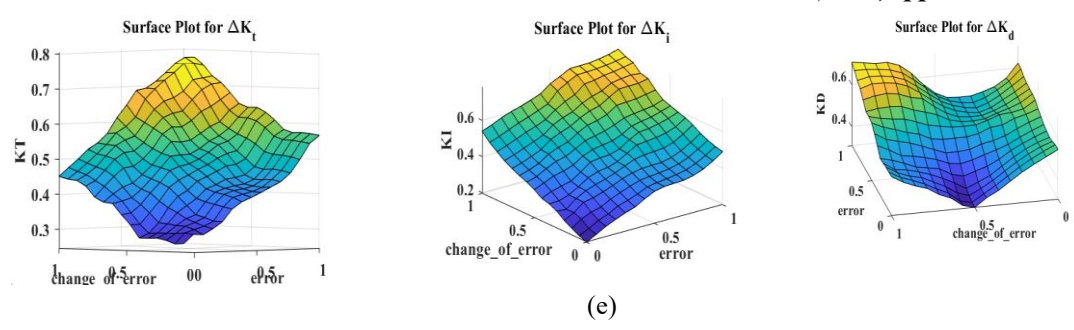


Fig. 3. (a) Block diagram of CMBO-HFF-2DoF-FOTIDC; (b) Fast fuzzy input1 (error) with respect to it's degree of membership; (c) Fast fuzzy input2 (rate of change of error) with respect to it's degree of membership; (d) Fast fuzzy outputs (ΔK_t , ΔK_i and ΔK_d) with respect to it's degree of membership; (e) Surface plot for fast fuzzy outputs (ΔK_t , ΔK_i and ΔK_d) with respect to inputs.

III.iv. Optimization of Control Parameters

The proposed HFF-2DoF-FOTIDC controller is tuned using two optimization techniques, namely CMBO.

III.iv.a. Cat and Mouse Optimization Algorithm (CMOA)

CMOA, inspired by cat and mouse behavior, optimizes solutions. It iteratively updates two populations: "cats" searching for promising areas and "mice" escaping them. Each individual represents a potential solution in the search space. The population is represented by a matrix (Equation (53)).

$$X = \begin{vmatrix} X_1 \\ \vdots \\ X_i \\ \vdots \\ X_m \end{vmatrix}_{N \times m} = \begin{vmatrix} X_{1,1} & \cdots & X_{1,d} & \cdots & X_{1,m} \\ \vdots & \ddots & \vdots & \ddots & \vdots \\ X_{i,1} & \cdots & X_{i,d} & \cdots & X_{i,m} \\ \vdots & \ddots & \vdots & \ddots & \vdots \\ X_{N,1} & \cdots & X_{N,d} & \cdots & X_{N,m} \end{vmatrix}_{N \times m}$$

$$(53)$$

where N represents the number of members in the population, m represents the number of search variables, X represents the population matrix, and $X_{i,d}$ represents the value of d^{th} the problem variable on the i^{th} search agent. Each member of the population has a value for the objective function. The value matrix for the objective function is represented by F. It is represented in the vector form by equation (54).

$$F = \begin{vmatrix} F_1 \\ \vdots \\ F_i \\ \vdots \\ F_N \end{vmatrix}_{N \times 1}$$

$$(54)$$

 $F_1 \cdots F_i \cdots F_N$ represents the objective function values for the 1^{st} , i^{th} and N^{th} search agents, respectively. Members are ranked by objective function, with the best at the top. Equation (55) shows the sorted population and objective function matrices.

$$X^{S} = \begin{vmatrix} X_{1}^{S} \\ \vdots \\ X_{i}^{S} \\ \vdots \\ X_{m}^{S} \end{vmatrix}_{N \times m} = \begin{vmatrix} X_{1,1}^{S} & \cdots & X_{1,d}^{S} & \cdots & X_{1,m}^{S} \\ \vdots & \ddots & \vdots & \ddots & \vdots \\ X_{i,1}^{S} & \cdots & X_{i,d}^{S} & \cdots & X_{i,m}^{S} \\ \vdots & \ddots & \vdots & \ddots & \vdots \\ X_{N,1}^{S} & \cdots & X_{N,d}^{S} & \cdots & X_{N,m}^{S} \\ \vdots & \vdots & \vdots & \vdots \\ F_{N}(max())_{N \times 1} \end{vmatrix}$$
(55)

 X^{s} represents the sorted population vector, while the sorted objective function vector is represented by F^s . $X_{i,d}^s$ represents the sorted value of d^{th} the problem variable on the ith search agent. The population matrix in CMOA, as mentioned earlier, is divided into two groups. This division is done as per the values of the objective function. The mice are assumed to have better objective function values, while the cats are assumed to have lower objective function values. The total population members N is divided amongst cats and mouse as N_c and N_m respectively. The populations of mice (M) and cats (C) are represented by equations (56-57).

$$M = \begin{vmatrix} M_{1} = X_{1}^{S} \\ \vdots \\ M_{i} = X_{i}^{S} \\ \vdots \\ M_{N_{m}} = X_{N_{m}}^{S} \end{vmatrix}_{N_{m} \times m} = \begin{vmatrix} X_{1,1}^{S} & \cdots & X_{1,d}^{S} & \cdots & X_{1,m}^{S} \\ \vdots & \ddots & \vdots & \ddots & \vdots \\ X_{i,1}^{S} & \cdots & X_{i,d}^{S} & \cdots & X_{i,m}^{S} \\ \vdots & \ddots & \vdots & \ddots & \vdots \\ X_{N_{m},1}^{S} & \cdots & X_{N_{m},d}^{S} & \cdots & X_{N_{m},m}^{S} \end{vmatrix}_{N_{m} \times m}$$
(56)

$$M = \begin{vmatrix} M_{1} = X_{1}^{S} \\ \vdots \\ M_{i} = X_{i}^{S} \\ \vdots \\ M_{N_{m}} = X_{N_{m}}^{S} \end{vmatrix}_{N_{m} \times m} = \begin{vmatrix} X_{1,1}^{S} & \cdots & X_{1,d}^{S} & \cdots & X_{1,m}^{S} \\ \vdots & \ddots & \vdots & \ddots & \vdots \\ X_{N_{m},1}^{S} & \cdots & X_{N_{m},d}^{S} & \cdots & X_{N_{m},m}^{S} \\ X_{N_{m},1}^{S} & \cdots & X_{N_{m},d}^{S} & \cdots & X_{N_{m},m}^{S} \end{vmatrix}_{N_{m} \times m}$$

$$C = \begin{vmatrix} C_{1} = X_{N_{m}+1}^{S} \\ \vdots \\ C_{i} = X_{N_{m}+k}^{S} \\ \vdots \\ C_{N_{C}} = X_{N_{m}+N_{C}}^{S} \end{vmatrix}_{N_{C} \times m} = \begin{vmatrix} X_{N_{m}+1,1}^{S} & \cdots & X_{N_{m}+1,d}^{S} & \cdots & X_{N_{m}+1,m}^{S} \\ \vdots & \ddots & \vdots & \ddots & \vdots \\ X_{N_{m}+k,1}^{S} & \cdots & X_{N_{m}+k,d}^{S} & \cdots & X_{N_{m}+k,m}^{S} \\ \vdots & \ddots & \vdots & \ddots & \vdots \\ X_{N_{m}+N_{C},1}^{S} & \cdots & X_{N_{m}+N_{C},d}^{S} & \cdots & X_{N_{m}+N_{C},m}^{S} \end{vmatrix}_{N_{C} \times m}$$

$$(56)$$

Equations (58-60) model cat behavior in updating search factors during the initial

phase.
$$C_{j}^{\text{new}}: C_{j,d}^{\text{new}} = C_{j,d} + r\left(m_{k,d} - I \times C_{j,d}\right)$$

$$\text{where}: j = 1: N_{c}, d = 1: m, k \in 1: N_{m}$$
(58)

$$I = round(1 + rand) \tag{59}$$

$$C_{j} = \begin{cases} C_{j}^{new}, |F_{j}^{C,new}\langle F_{j}^{C}| \\ C_{i}, |else \end{cases}$$

$$(60)$$

where C_j^{new} is the newest of j^{th} cat and $C_{j,d}^{new}$ is the value of the d^{th} problem variable obtained by the j^{th} cat, r is a random number having values between 0 and 1, $m_{k,d}$ is the d^{th} dimension of the k^{th} mouse, $F_j^{C,new}$ is the objective function value of the obtained after the new status of the jth cat. In the second phase, the escape of the mice to havens is modelled. The positions of the haven are created randomly based on prior knowledge about the patterns of different members. Mice are always required to take refuge in these havens. The position updation of mice is mathematically modeled and represented by equation (61-62).

$$\left. \begin{array}{l} H_{i}:h_{i,d} = X_{l,d} \\ M_{i}^{new}:M_{i,d}^{new} = M_{i,d} + r \Big(h_{i,d} - I \times C_{i,d}\Big) \times sign\Big(F_{i}^{m} - F_{i}^{H}\Big) \\ \text{where}:i = 1:N_{m}, d = 1:m, l \in 1:N \end{array} \right)$$

$$M_{i} = \begin{cases} M_{i}^{new}, |F_{i}^{M,new}\langle F_{i}^{M} | \\ M_{i}, |else \end{cases}$$

$$(62)$$

where M_i^{new} is the newest of i^{th} mouse, and $M_{i,d}^{new}$ is the value of the d^{th} problem variable obtained by the i^{th} mouse, $h_{i,d}$ is the d^{th} dimension of the i^{th} cat, $F_i^{M,new}$ is the objective function value obtained after the new status of the i^{th} mouse. Once all the optimization function values are updated and the best value is noted, the algorithm enters the next iteration and follows the steps as mentioned in eqn (56-66). The optimization stops once the stopping criteria is reached. The stopping criteria can be the maximum number of iterations, allowable error limits, or the same error values for successive iterations. The flowchart explaining the optimization process is depicted in fig.3.

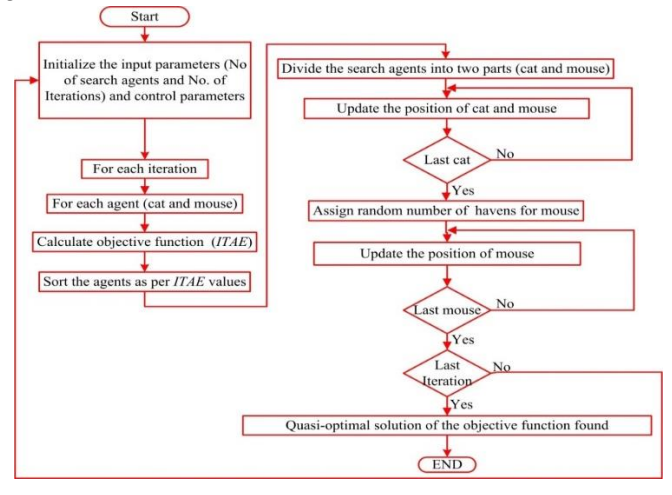


Fig. 3. Flowchart for CMOA technique

Figure 3 illustrates the flowchart for the Cat Mouse Optimization Algorithm (CMOA) technique, outlining the step-by-step process of optimization. The flowchart begins with the initialization stage, where algorithm parameters, including population size, search space, and termination criteria, are defined. Next, the random generation of cat and mouse agents within the solution space takes place, ensuring diversity in the initial population. The algorithm then enters the evaluation phase, where the fitness of each agent is assessed based on a predefined objective function, such as minimizing power loss or improving system stability. Following evaluation, the exploration and exploitation phases begin, where the cat (predator) pursues the mouse (prey) using adaptive search strategies. The algorithm dynamically adjusts the movement of agents based on their fitness values, enhancing convergence toward the optimal solution. The updating phase then refines the positions of the agents, balancing exploration (searching new areas) and exploitation (refining the best solutions). The stopping

criteria check determines whether the optimization process should continue or terminate. If the maximum number of iterations is reached or the fitness function stabilizes, the algorithm proceeds to the final selection phase, where the best solution is extracted. This optimized solution is then applied to GISIS control, improving performance parameters such as voltage stability, reduced ripple, and enhanced energy efficiency. By following this structured approach, the CMOA technique ensures fast and accurate convergence to optimal control parameters, making it a reliable method for enhancing smart inverter systems and other power optimization applications.

IV.i. Closed-loop RLC

Solar panels' low voltage necessitates boosting before utilization. RLC circuits, controlled by the 2DoF-FOTIDC at 40 kHz, achieve this. While typical converters target 48V, a 50V output enhances performance, as exemplified in Figure 9.

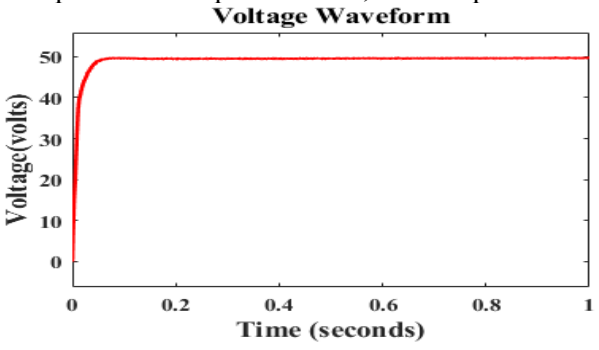
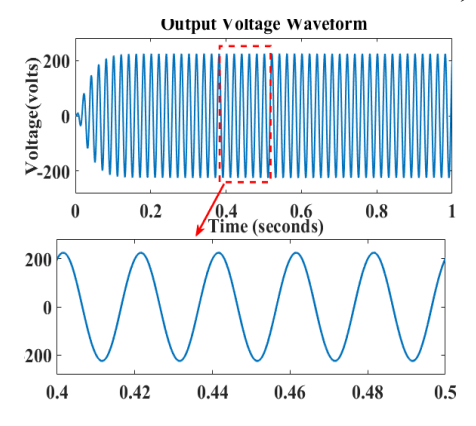


Fig. 9. RLC DC output voltage

Figure 9 illustrates the DC output voltage of the Relift Luo Converter (RLC), demonstrating its capability to provide a stable and enhanced DC voltage with minimal ripple. The plot highlights how the RLC topology improves voltage gain and efficiency by effectively reducing high-frequency oscillations through its inductor-capacitor filtering mechanism. The steady-state output confirms the converter's ability to boost and regulate voltage efficiently, making it highly suitable for Grid-Integrated Smart Inverter Systems (GISIS) and renewable energy applications requiring high power quality.

IV.ii. Closed-loop 15L-SMMI

The 15L-SMMI inverter converts DC voltage to AC, supplying 220V AC to a 100 + 240e-3j Ω load. The load consumes 2A current and 360W of power. Figure (10-12) illustrates the inverter's V_{inv} , load current (I_{inv}) and power consumption (P_{inv}).



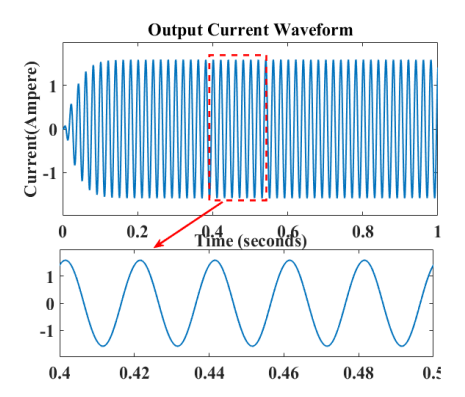


Fig. 10. V_{inv} of CMBO-based 15L-SMMI

Fig. 11. I_{inv} of CMBO-based 15L-SMMI

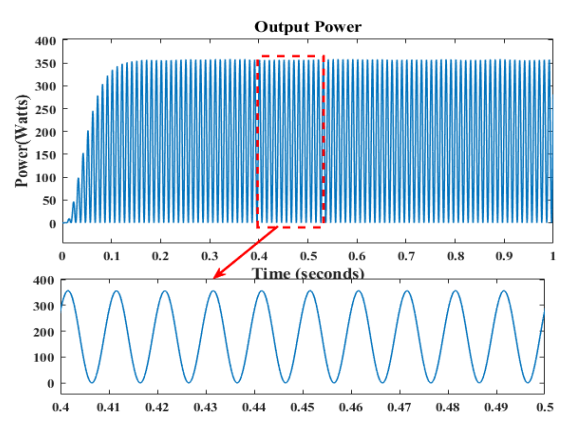
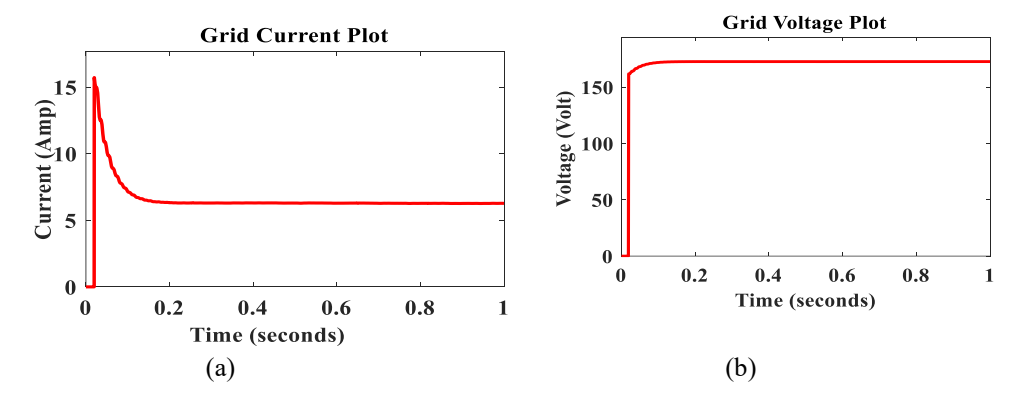


Fig. 12. P_{inv} of CMBO-based 15L-SMMI

A three-terminal transformer supplies a 12kW load, drawing power from GISIS. The GISIS supplies 162.5V RMS. The grid supplies 6.3A, the inverter 11.63A, resulting in 169.5V and 8.134A at the load (Figure 13).



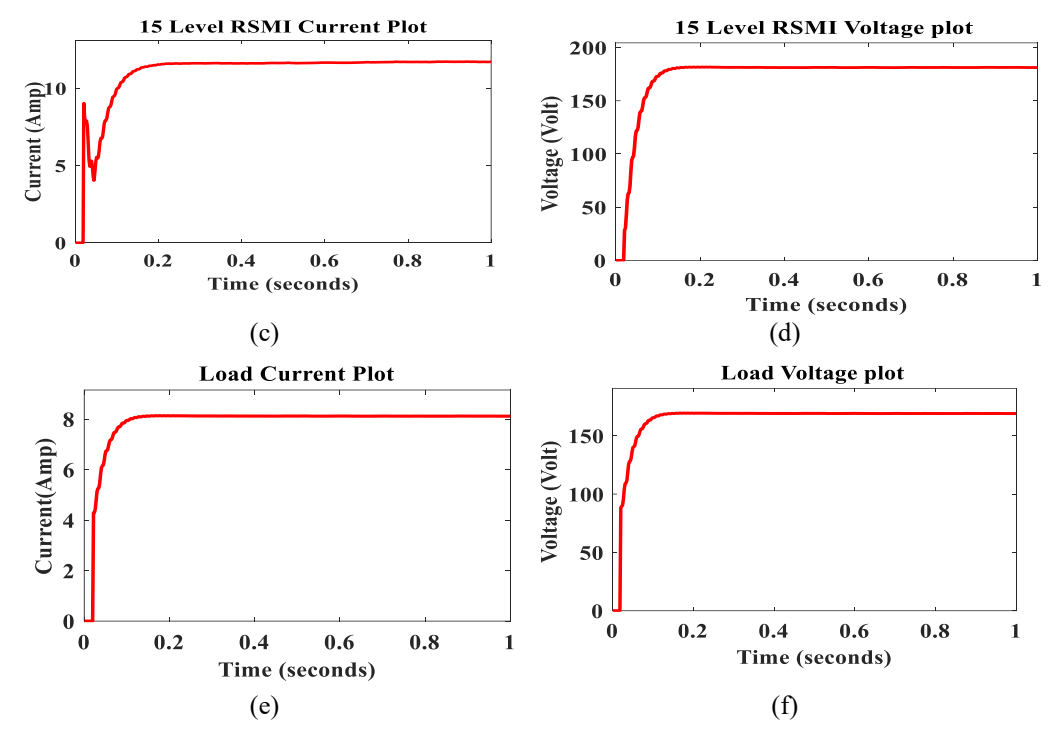


Fig. 13. Plot for (a) Grid current; (b) Grid voltage; (c) I_{inv} ; (d) V_{inv} ; (e) Load current; (f) Load voltage.

IV.iii. Robustness Analysis

The proposed GISIS demonstrates robustness against rapid changes in operating conditions like temperature and irradiance. This is verified by observing minimal impact on system responses (voltage, current, and power) during these changes. Temperature variations within the optimal photovoltaic range (293.15 - 321.15 K) have minimal impact, as shown in Figure 14(a-c). Voltage deviation is 0.162% (0.26 volts), current deviation is 0.074% (0.001 amp), and power deviation is 0.645% (248.3 - 294.8 watts). Similarly, irradiance changes from seven hundred W/m² to one thousand sixty-one W/m² (optimal band) result in minor variations: voltage deviation of 2.18% (3.52 volts), current deviation of 0.022% (0.003 amp), and power deviation of 4.03% (10 watts). Figure 14(d-f) depicts these variations. These minimal changes in response to environmental fluctuations demonstrate the proposed GISIS's robustness.

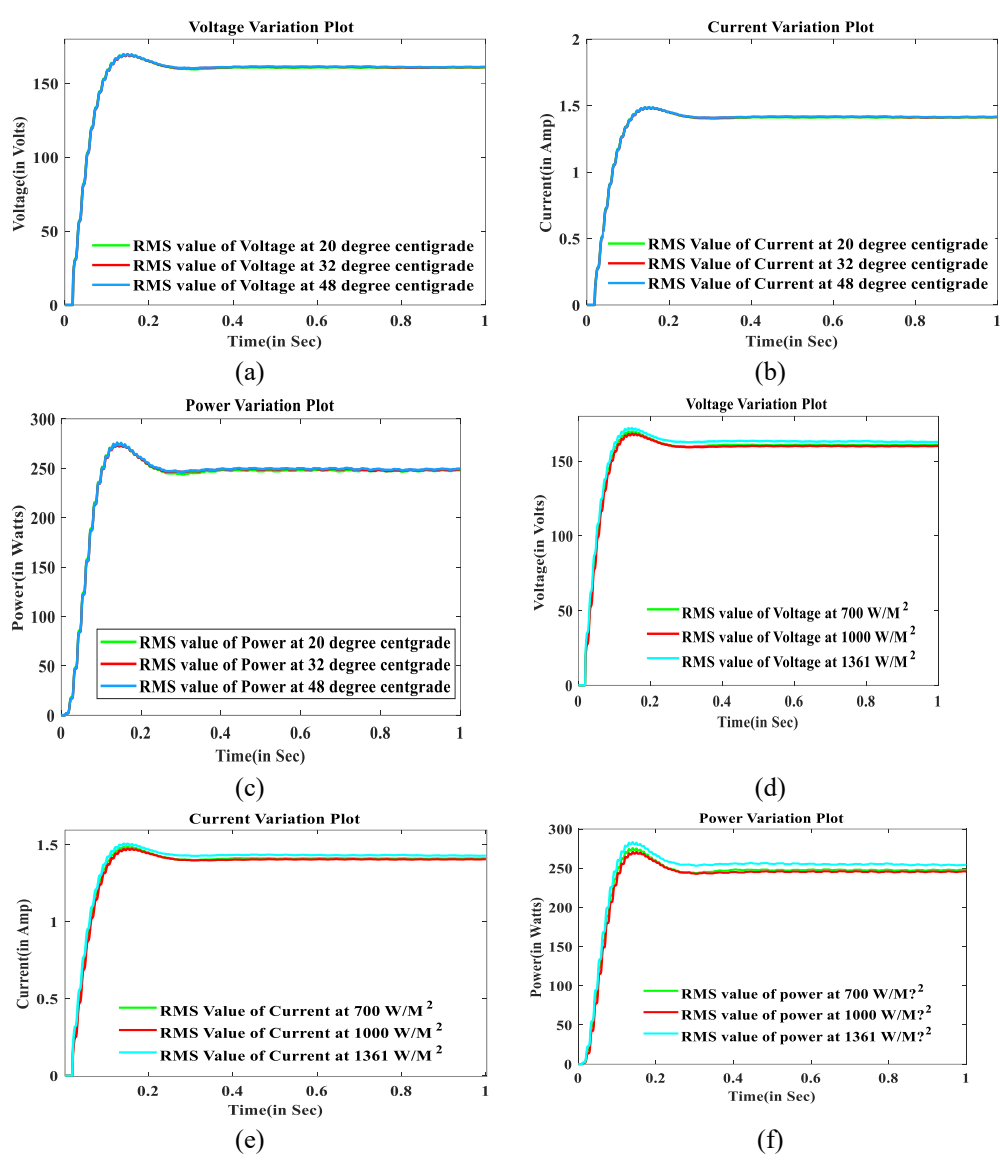


Fig. 14. 15L-SMMI performance under varying conditions: **Temperature:** (a) Output voltage, (b) Output current, (c) Output power. **Irradiance:** (d) Output voltage, (e) Output current, (f) Output power.

IV.iv. Stability of Hybrid-Fuzzy-Tilt-Integral-Derivative-Controller with Filter Frequency domain study validates the proposed model's stability. Bode plots in Figure 15(a-b) illustrate the system's behavior under open and closed-loop conditions. Figure 15(a) shows that the open-loop system exhibits instability, characterized by a non-converging and potentially oscillating response. Conversely, Figure 15(b) demonstrates the system's improved stability with the CMBO-HFF-2DoF-FOTIDC control scheme. The response exhibits superior smoothness and signifies faster settling time, indicating quicker stabilization. However, a minor peak observed in the response (Figure 15(b)) warrants further investigation. While this peak might not

directly compromise stability, understanding its origin and potential impact on the system's performance under various conditions is crucial. The adaptive nature of the proposed control strategy, utilizing CMBO-HFF-2DoF-FOTIDC, reduces output nonlinearities, minimizing minor peaks.

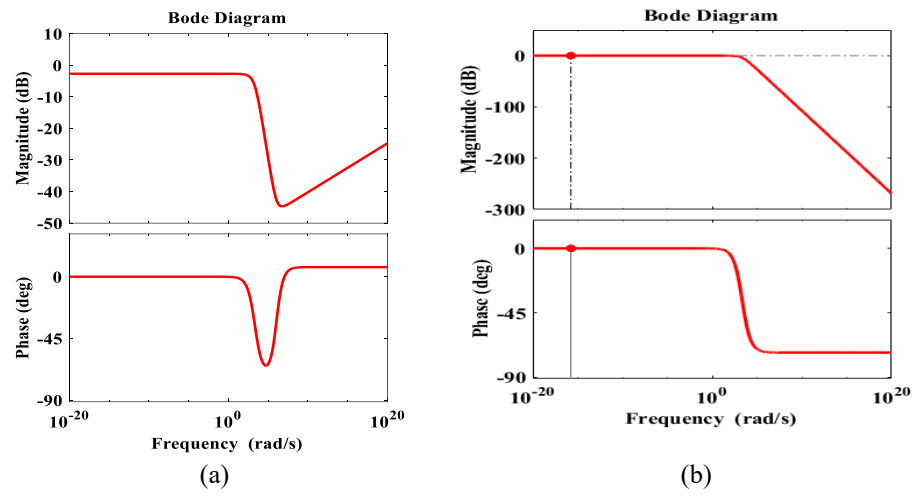


Fig. 15. (a) Open-loop Bode plot; (b) Bode plot.

IV.v. Comparative Analysis

Compared to other modern controllers, the proposed CMBO-HFF-2DoF-FOTIDC based GISIS demonstrates superior performance, as shown in Table 5. For grid-connected systems, the IEEE-519 standard mandates total harmonic distortion (THD) below 5% for 30 cycles. The proposed model achieves a current THD of 0.61% (Figure 16), bettering this benchmark.

Table 5: Comparative study of CMBO-HFF-2DoF-FOTIDC based GISIS with other control techniques

Metric	Solar- Photovoltaic Model with ANN controller [3]	Solar- Photovoltai c Model with ANFIS controller [4]	Solar- Photovoltai c Model with Hysteresis control [5]	Solar- Photovoltaic Model with DSP-based controller [6]	Solar- Photovoltaic Model with DSP-based controller [7]	Solar- Photovoltaic Model with CMBO-HFF- 2DoF- FOTIDC
thdi	2.75%	1.17%	1.72%	0.9%	1.23%	0.61%
Switching Frequency		30 kHz	30 kHz	20 kHz	20 kHz	40 kHz
stability	inferior	inferior	inferior	inferior	inferior	superior
Robust	inferior	inferior	inferior	inferior	inferior	superior

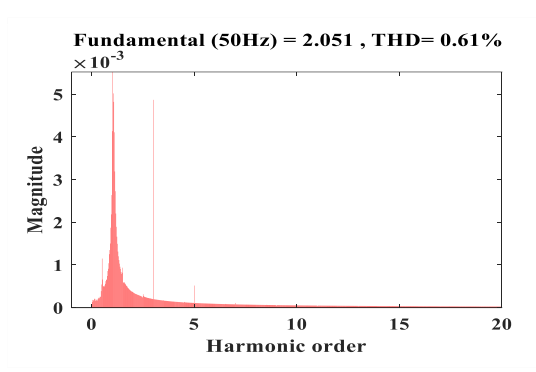


Fig. 16. Current harmonic plot proposed system

V. Conclusions

CMBO-HFF-2DoF-FOTIDC, a novel control strategy, is proposed in the purview of this manuscript and is based on the hybridization of fuzzy and fractional order controller concepts. The CMBO-HFF-2DoF-FOTIDC approach treats all control parameters as dependent on the error signal. A control approach is employed solar inverter system and found to justify its better performance under fluctuations in solar irradiance and temperature. The control performance is enhanced by using CMBO-HFF-2DoF-FOTIDC. The comparative findings demonstrate the proposed control technique's performance superiority, stability, reliability, robustness under parameter variation, and disturbances as compared to ANN, ANFIS, Hysteresis control, and DSP-based controller. The proposed control approach has enhanced performance in terms of stability, accuracy, and capabilities to handle disturbances and uncertainties, which justifies the real-time application.

Conflict of Interest

The authors declare that there is no conflict of interest regarding the publication of this manuscript.

References

- I. Abualigah, L., & Gandomi, A. H. Aquila optimizer: a novel meta-heuristic optimization algorithm. *Computers & Industrial Engineering*, 157(1), 1–25. 2021.
- II. Andela, M., & Salkuti, S. R. Solar GISIS-based reduced switch multilevel inverter for improved power quality. *Clean Technologies*, 4(1), 1–13. 2022.

- III. Dheeban, S. S., & Krishnaveni, L. Performance improvement of Photo-Voltaic panels by Super-Lift Luo converter in standalone application. Materials Today: Proceedings, 37(1), 1163–1171. 2021.
- IV. Guohua, L., & Feng, L. Single-Phase Voltage Source Multi-Level Inverter Hysteresis RPPPWM Reconfigurable Fault-Tolerant Control Method. Energies, 15(7), 2557. 2022.
- V. Lin, H., He, X., et al. A Simplified 3-D NLM-Based RPPPWM Technique With Voltage-Balancing Capability for 3LNPC Cascaded Multilevel Converter. *IEEE Transactions on Power Electronics*, 35(4), 3506–3518. 2020.
- VI. Logasri, R. Study on Performance Analysis of Luo Converter with Fuzzy Controller. *Turkish Journal of Computer and Mathematics Education* (*TURCOMAT*), 12(9), 2793–2798. 2021.
- VII. Logeswaran, T., Senthilkumar, A., & Karuppusamy, P. Adaptive neuro-fuzzy model for Grid-Interfaced GISIS. *International Journal of Fuzzy Systems*, 17(4), 585–594. 2015.
- VIII. Nguyen, P. C., & Nguyen, D. T. A new decentralized space vector PWM method for multilevel single-phase full bridge converters. *Energies*, 15(3), 1010. 2022.
 - IX. Palanisamy, R., & Vijayakumar, V. Artificial neural network based RPPPWM for five level cascaded H-bridge inverter fed grid connected PV system. *Journal of Intelligent and Fuzzy Systems*, 39(6), 8453–8462. 2020.
 - X. Patra, A. K., & Nanda, A. Implantable Insulin Delivery System Based on the Genetic Algorithm PI Controller (GA-PIC). In *Advances in Intelligent Computing and Communication* (pp. 243–252). Springer, Singapore. 2021.
 - XI. Patra, A. K., & Rath, D. Design of PV System based on 3-Degree of Freedom Fractional Order Tilt-Integral-Derivative Controller with Filter. *J. Inst. Eng. India Ser. B*, 103(1), 1533–1548. 2022.
- XII. Patra, A. K., & Rout, P. K. Design of artificial pancreas based on the SMGC and self-tuning PI control in type-I diabetic patient. *International Journal of Biomedical Engineering and Technology*, 32(1), 1–35. 2020.
- XIII. Rai, A., & Das, D. K. The development of a fuzzy tilt integral derivative controller based on the sailfish optimizer to solve load frequency control in a microgrid incorporating energy storage systems. *Journal of Energy Storage*, 48(1), 1–30. 2022.
- XIV. Rath, D., Kar, S., & Patra, A. K. Harmonic Distortion Assessment in the Single-Phase Photovoltaic (PV) System Based on SPWM Technique. *Arab Journal of Science and Engineering*, 46(4), 9601–9615. 2021.
- XV. Rezaei, M. A., & Khooban, M. H. A New Hybrid Cascaded Switched-Capacitor Reduced Switch Multilevel Inverter for Renewable Sources and Domestic Loads. *IEEE Access*, 10(1), 14157–14183. 2022.

- XVI. Singh, A., & Udhayakumar, R. Asymptotic stability of fractional order (1, 2] stochastic delay differential equations in Banach spaces. *Chaos, Solitons & Fractals*, 150(1), 111095. 2021.
- XVII. Wang, P., & Montanari, G. C. Considering the Parameters of Pulse Width Modulation Voltage to Improve the Signal-to-Noise Ratio of Partial Discharge Tests for Inverter-Fed Motors. *IEEE Transactions on Industrial Electronics*, 69(5), 4545–4554. 2021.